Lab on a Chip

Biologically Inspired Micro-Robotic Swimmers Remotely Controlled by Ultrasound Waves

Journal:	*Lab on a Chip*
Manuscript ID	LC-ART-06-2021-000575.R1
Article Type:	Paper
Date Submitted by the Author:	23-Aug-2021
Complete List of Authors:	Luo, Tao; Xiamen University, Mechanical and Electrical Engineering Wu, Mingming; Cornell University, Department of Biological and Environmental Engineering

Lab on a Chip

ARTICLE

Biologically Inspired Micro-Robotic Swimmers Remotely Controlled by Ultrasound Waves †

Received 00th January 20xx,
Accepted 00th January 20xx

DOI: 10.1039/x0xx00000x

www.rsc.org/

Tao Luo[a,b] and Mingming Wu*[a]

We 3D print micro-robotic swimmers the size of animal cells using a nanoscribe. The micro-swimmers are powered by the microstreaming flows induced by the oscillating air bubbles entrapped within the micro-robotic swimmer. Previously, micro-swimmers propelled by acoustic streaming require the use of the magnetic field or additional ultrasound transducer to steer its direction. Here, we show a two bubble based micro-swimmer that can be propelled and steered entirely by one ultrasound transducer. The swimmer displays boundary following traits similar to those biological swimmers that are known to be important for performing robust biological function. The micro-robotic swimmer has the potential to advance the current technology in targeted drug delivery and remote microsurgery.

Introduction

"Many of the cells are very tiny, but they are very active; they manufacture various substances; they walk around; they wiggle; and they do all kinds of marvelous things---all on a very small scale". The seminal speech *There's plenty of room at the bottom* given by Richard Feynman in 1959 is still inspiring us today to make micro-scale robotic swimmers, similar to bacteria and sperm, that has the ability to reach targeted locations within a fluidic environment in a robust way [1]. In parallel to the scientific challenge of making small maneuverable robotic swimmers (i.e. micro-swimmer), this research direction is also motivated by the rapid development of biomedical field and its applications in targeted drug delivery and remote microsurgery [2–4].

Broadly speaking, micro-robotic swimmers have two ways to obtain their energy [5]: on-board energy sources including those realized through chemical [6,7] and biological [8,9] reactions, and off-board energy sources including those that can be coupled to the swimmer via electric [10], optical [11,12], magnetic [13–17], and acoustic [18–22] fields. Trading among robustness, controllability and biocompatibility, ultrasound and magnetic field have emerged as two most commonly used energy sources for remotely controlled micro-swimmers in the context of biomedical applications [23–25]. They capitalize the existing FDA approved technology including MRI and ultrasound imaging that are safe for clinical use. Here, we will focus on ultrasound powered micro-swimmer for its flexibility in material choice, small size instrument, as well as its potential to be integrated with the existing acoustic imaging system [26] for image-guided control of micro-swimmers inside human body [27].

To gain control of the *speed* and the *direction* of the swimmer is the key step for developing a micro-robotic swimmer. Extensive progresses have been made in creating micro-robotic swimmer that uses a propulsion force from acoustic streaming -- a fluid flow with two symmetric vortices created in the rear of an oscillating micro-bubble [28–34]. Microbubble based microswmmers are advantageous in biomedical applications due to its material biocompatibility [35]. In these studies, the speed of the micro-swimmer is shown to be easily controlled by acoustic waves ranging from audible to ultrasound frequency [30,31,36]. An existing hurdle for the development of an autonomous micro-swimmer is the ability to remotely steer the direction of the swimmer. Currently, magnetic field or an additional acoustic transducer have been used to steer the micro-robotic swimmer propelled by acoustic streaming [33,36–39]. However, the inclusion of magnetic field or additional acoustic wave source increases the complexity of the control mechanism, size of the instrument, range of materials used, and thus limiting their applications. The challenge is whether one can control the speed and direction of a robotic micro-swimmer using one ultrasound transducer. Recent work at audible frequency region has shown promises [38,40].

This paper presents the first micro-robotic swimmer that can be remotely powered and steered using one ultrasound transducer. In addition, the micro-swimmer displays boundary following characteristics, a trait commonly seen in biological pusher micro-swimmers.

Results and Discussion

Design and working principle of the micro-robotic swimmer

The proposed micro-swimmer is triangular in shape with two identical micrometer scale air bubbles trapped in the back (Fig. 1A). Each air bubble can be excited via ultrasonic waves. Upon resonance, each of the two air bubbles creates a streaming flow through an opening, and together, they propel the micro-swimmer forward (Fig.

[a] Departments of Biological and Environmental Engineering, Cornell University, Ithaca, NY 14853, USA.
*E-mail: mw272@cornell.edu
[b] Department of Mechanical and Electrical Engineering, Xiamen University, Xiamen 361005, China.
† Electronic supplementary information (ESI) available.

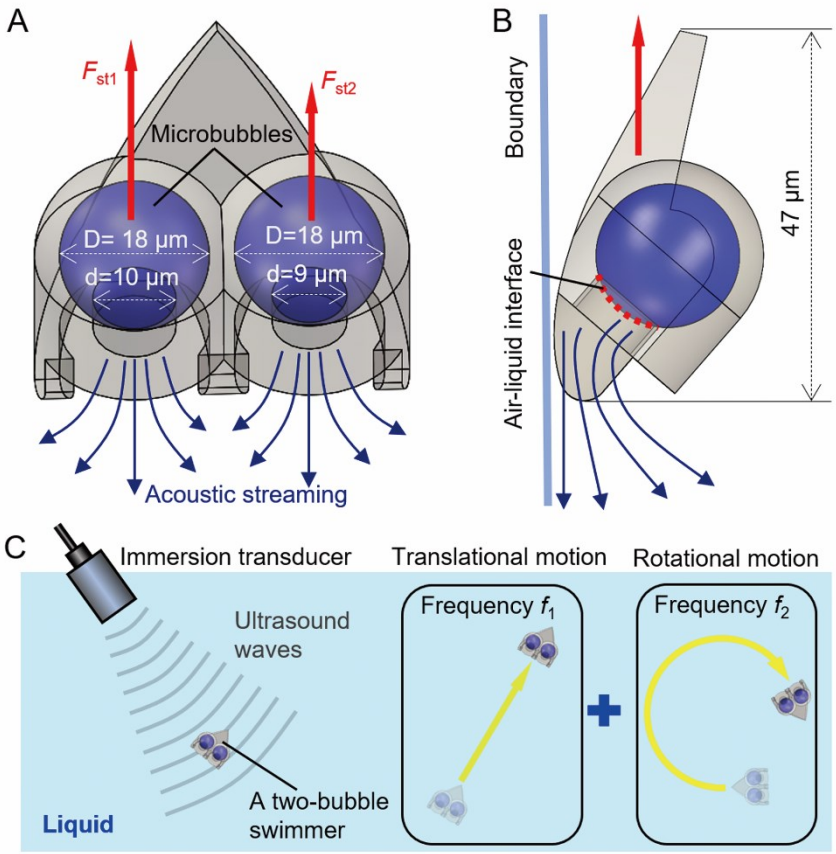

Fig. 1 Design principles of a remotely controlled micro-swimmer. (A, B) Illustration of the front (A) and side (B) view of a two-bubble micro-swimmer. Two microbubbles of the same diameter (D =18 µm) were trapped in the two cavities with different sizes of opening towards the fluid environment (d = 10 and 9 µm). Ultrasonic excitation of the microbubbles generates a streaming flow, which propels the swimmer forward. (C) Illustration of the control mechanism of the micro-robotic swimmer. An immersion ultrasound transducer is used to power and steer the micro-swimmer in a fluidic environment remotely. The swimmer swims in a straight line when the streaming forces from the two bubbles are the same, and rotates when they are not. Here, frequency is tuned to allow the swimmer to swim in either a straight line or a circle.

1A and B). It is important to note that the resonance frequency of the air bubble depends sensitively on the diameter of the air bubble *D* as well as the opening diameter *d* (Fig. 1A) [36]. We choose to have two air bubbles with the same diameter *D* but different opening (*d* =10 µm versus 9 µm in Fig. 1A), to allow for the selective excitation of microbubbles by tuning the frequency of the ultrasound waves. This feature allows us to control the locomotion of the swimmer, either following a straight path or a circle, using the ultrasound frequency (Fig. 1C).

To guide the design of the microrobot, we estimated the resonance frequency of the microbubbles. For a partially exposed air bubble as shown in Fig. 1A, the resonance frequency can be estimated as [36]:

$$f_0 = \frac{4}{\pi d^2}\sqrt{\frac{2\sigma D}{\rho}} \quad (1)$$

where $\sigma \sim 69.5\, mN \cdot m^{-1}$ is the surface tension at the air-liquid interface and $\rho = 1010 kg/m^3$ is the density of the surrounding liquid. Eqn. 1 indicates that the resonance frequency of a partially exposed microbubble is sensitively dependent on the size of the opening, and it is proportional to $1/d^2$. This is the key factor that we designed the micro-swimmer with two bubbles of the same diameter *D* but different opening *d*. This allows for a differential resonance frequency control of the two bubbles, while maintaining minimal left-right asymmetry of the swimmer. This feature is critical for the eventual robust steering of the swimmer using ultrasound frequency. We note that Eqn 1 is an estimate and it assumes that the bubble behaves adiabatically without thermal losses, which can not be neglected due to the small size of the bubble[41].

Frequency dependent microstreaming of a single air bubble micro-swimmer

For the purpose of demonstrating the microstreaming behaviour of an oscillating air bubble, we made a simpler swimmer with a single air bubble. An air bubble of diameter *D* was trapped in a cavity similar to the design of the two bubble swimmer and has a partial air-liquid interface with a circular opening of diameter *d* (Fig. 2A). To facilitate flow visualization, the swimmer was anchored on a substrate and submerged in fluid embedded with 1 µm diameter fluorescence marker beads. A pair of vortices appear when frequency is tuned to the resonance of the oscillating bubble as shown in Fig. 2B. The pair of vortices observed here is consistent with the streaming pattern reported in previous work [32,36,42].

The frequency dependency of the acoustic streaming on *d* is clearly demonstrated in Fig. 2B and Movie S1. Here, we have two single bubble micro-swimmers with same bubble diameter *D*, but different opening *d*. Fig. 2B shows that the swimmer with *d* = 8 µm exhibits microstreaming at ultrasound frequency of 396kHz. The swimmer with *d* = 10 µm, however, exhibits microstreaming at ultrasound frequency of 300 kHz. This observation is consistent with Eqn. 1 where the resonance frequency is estimated to be proportional to $1/d^2$. We note that the single bubble swimmer is directly printed onto the fused silica substrate initially, and it is observed to swim away when detached from the substrate using a pipette tip[36].

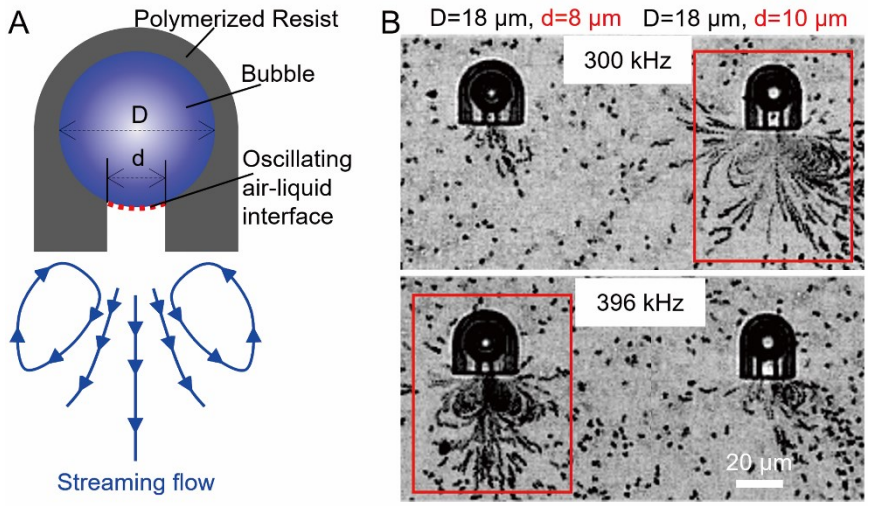

Fig. 2 Selective excitation of the streaming flow using different ultrasound frequencies demonstrated by anchored single bubble swimmers. (A) Illustration of a one-bubble swimmer along with the acoustic streaming flow field induced by the oscillating microbubble. (B) The streaming magnitude under a specific ultrasound frequency depends on the size of the air-liquid interface, or the diameter of the opening d. At 300kHz, swimmer with d= 10 μm has stronger streaming flow, while at 396 kHz, swimmer with d=8 μm results in stronger streaming. The image is superimposed by 21 images taken consecutively with 50 ms apart.

Micro-robotic swimmers always swim along a boundary, a trait commonly seen in biological micro-swimmers

To test the swimming behavior of the two-bubble swimmers, we enclose them in a microfluidic channel, and subject them to the ultrasound waves emitted by an immersion ultrasound transducer (See Fig. S1). When the ultrasound transducer is turned on, the swimmers first adjust their attitude quickly, in about 100 ms, to a final position (Fig. 3A, B and Movie S2), and then swim along a boundary, either close to a substrate surface or a channel boundary (Fig. 3). Time sequence micrographs of the micro-swimmer imaged from below (taken by an inverted microscope) show that the protrusion of the swimmer body at the rear is visible at t = 0, and disappears at t = 150 ms due to the attitude adjustment. Fig. 3D and Movie S3 show that the micro-swimmer is always in focus during the 16 s of translational movement. These images are taken with 10X objective lens indicating that the swimmer is close to the substrate within a few micrometers during the course of at least 16 s. In the case when a micro-swimmer approaches a wall of a channel, we find that it always swims along the wall of a microfluidic channel, even when the wall undergoes a bend as seen in Fig. 3E and Movie S4.

A force diagram analysis of the swimmer (Fig. 3C) shows that the near boundary swimming behavior is likely caused by the hydrodynamic interactions between the swimmer and the boundary. Fig. 3C is a force diagram of the micro-swimmer, in which the micro-swimmer experiences a streaming force F_{st} due to the streaming vortices in the fluids, a Bjerknes force F_{SB} due to the hydrodynamic interactions between the oscillating bubble and the boundary [43], and a resistive force F_R, which consists of the drag force and the friction force. We assume that the weight and the buoyancy force of the swimmer cancel. Also, we assume that the resistive force is comparable to the x-component of the streaming force leading to a constant motion soon after the acoustic wave is turned on. We note that the importance of the design for a curved bottom, such that the force generated by the acoustic streaming is not perpendicular to the substrate. The curved bottom design has two advantages that allows for robust and efficient control: (i) it creates the x-component of streaming force which propels the swimmer forward; (ii) it allows for the reduced contact area between the swimmer and the boundary, minimizing the friction and enhancing propulsion efficiency.

The attractive secondary Bjerknes force, which comes from the hydrodynamic interaction between the oscillating bubble and the solid boundary that reflects the acoustic waves [44], is important in the attitude adjustment of the micro-swimmer when interacting with a boundary. The secondary Bjerknes force experienced by a bubble near the boundary/substrate can be estimated as $F_{SB} \sim 64\pi f^2 \rho \epsilon^2 D^6 / L^2$, where L is the distance between the oscillating bubble and the boundary/substrate, f is the frequency of the ultrasound wave, and ϵ is the relative oscillation amplitude scaled by the diameter of the bubble [32,34]. Since we know that the streaming force of oscillating bubble in free space, $F_{st} \sim 16\epsilon^2 \rho D^4 f^2$, the ratio of the secondary Bjerknes force and streaming force for the volume resonance mode scales as:

$$\frac{F_{SB}}{F_{st}} \sim 4\pi D^2 \cdot \frac{1}{L^2} \quad (2)$$

The secondary Bjerknes force is inversely proportional to the square of the distance between the bubble and the substrate/boundary. This means that the attractive secondary Bjerknes force becomes larger as the swimmer approaches the substrate/boundary, which is consistent with the boundary following trait of the swimmer observed in experiments (Fig. 3D, E). This relatively large attractive force also results in the automatic attitude adjustment shown in Fig. 3A-B as the swimmer swims close to a surface. We note that Eqn 2 is a very crude estimate similar to a dimensional analysis. For a more accurate calculation, one needs to consider the near wall effect when computing streaming force since the shedding vortices are larger than the distance of the swimmer to the wall, as well as the fact that the bubble is enclosed within a cavity with an opening.

Swimming along a boundary is a key characteristics of a pusher micro-swimmer in biology including *E.coli* bacteria and mammalian sperm, and it is important for their ability to spread and also to reach targeted locations [45,46]. It is well known that a pusher swimmer prefers to swim along a boundary due to its hydrodynamic interactions with the boundary [47]. Theoretically, the requirement for boundary following is that the micro-swimmer swims by pushing the fluids, and the body of the swimmer has a front-back asymmetry. The two-bubble swimmer falls into this category in that the swimmer is propelled by the shedding vortices, and it has a triangular shape, narrow in the front and wide in the back. We note that the ability to

always follow a boundary is important for biomedical applications of a robotic swimmer as well. For example, the swimmers can be easily controlled to navigate in a vascular system following the contour of the vasculature.

It is interesting to note that robotic and biological swimmer both use the spatial asymmetry of the propelling and resistive force to follow a boundary. In contrast to the biological swimmer, the robotic swimmer also uses Bjerknes force to get close to a wall. For biological swimmer, it swims in random motion, and follows the wall only when it accidentally swims close to it. In this sense, the robotic swimmer has a more robust control for following a boundary than that of biological swimmer. We also note that secondary Bjerknes force could be affected by the acoustic properties of the wall, in particular, when the wall is made of soft tissue. In the future, it will be interesting to see how robotic swimmers swim in a more physiologically realistic environment, e. g. a microfluidic channel made of soft materials and with fluid flows.

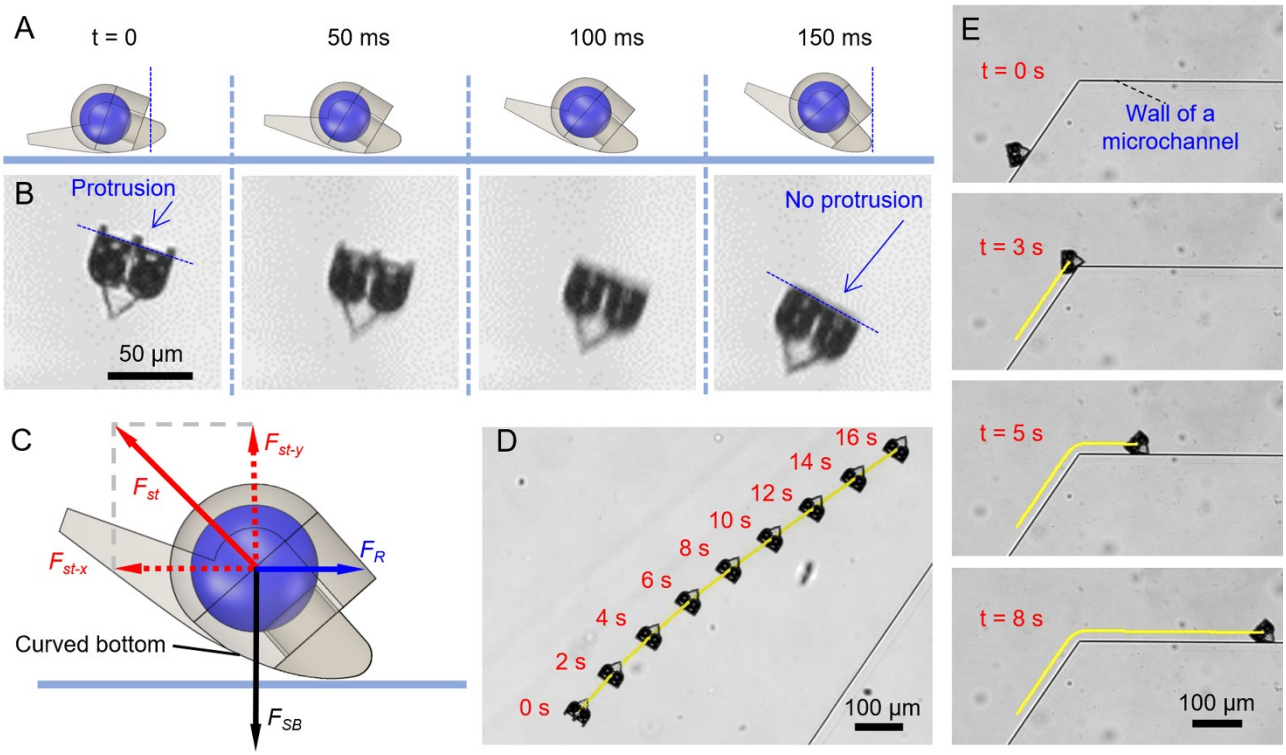

Fig. 3 The micro-swimmer always swims along a boundary. (A) A schematic drawing of the micro-swimmer showing its initial attitude (side view) adjustment when the ultrasound is turned on at t =0; (B) Micrographs taken by an inverted microscope (10X Objective), showing the attitude adjustment process (bottom view). Note the protrusion on the back side of the swimmer is visible when t=0; and not visible at t=150 ms due to the attitude adjustment. (C) Force diagram of a micro-swimmer with the curved bottom. F_{st} is the streaming force, F_{st-x} and F_{st-y} are the force components of the streaming force in horizontal and vertical direction, respectively; F_{SB} is the attractive secondary Bjerknes force, and F_R is the resistive force that includes drag and friction force. (D) Micro-swimmer swims and stays close to a substrate. A super imposed image using a time series of 9 images shows that a micro-swimmer is always in focus during the 16 s filming time. This indicates that the swimmers always stay close to the substrate. (E) Locomotion guided by the wall of the microfluidic channel. A time image series shows that the swimmer always swims along the wall of a microfluidic channel. All the swimmer shown above has two bubbles with D= 18μm, d = 10 μm for left bubble and 9 μm for right bubble. The driving frequency is 346 kHz and the peak-to-peak voltage of the function generator is 300 mV.

Ultrasound frequency and amplitude controls the locomotion of the micro-swimmer

The motion of the micro-swimmer can be altered between straight and rotational by changing the frequency of the ultrasound wave. For the micro-swimmer with geometry shown in Fig. 1A, the micro-swimmer moves in a nearly straight line when the ultrasound frequency is between 300 and 345 kHz; and rotates when the ultrasound frequency is between 215 and 235 kHz. Fig. 4A, B and Movie S5 show an example where a micro-swimmer moves in a straight line at ultrasound frequency 301 kHz; while it moves in circles when at 234kHz. We note that ultrasound frequency is swept from 100 to 1000 kHz in steps of 1 kHz to find the resonant frequencies of the micro-bubbles in a typical experiment.

The speed of the swimmer is found to be linearly proportional to the voltage squared for micro-robotic swimmers (Fig. 4C). Here, the voltage is the voltage input to the function generator (Fig. S1) that connects to the ultrasound transducer via a power amplifier. This linear relation is consistent with the theory that the streaming force F_{st} is proportional to ultrasound amplitude squared and the ultrasound wave amplitude is proportional to the voltage input to the ultrasound transducer [31,33]. Fig. 4C shows that when the voltage increases from 100 to 300 mV, the speed of the translational motion of the micro-swimmer increases from 5 to 66 μm/s, and the speed of the circling swimmer increases from 15 to 130 μm/s. The slight deviation from the linear function in Fig. 4C can be caused by the hydrodynamic interactions between the swimmer and the boundary due to the near surface swimming. The maximum translational speed of the micro-swimmer is 66 μm/s at 300 mV, which is about 1.4 body length per second. The maximum speed of the circling swimmer is 130 μm/s at 300 mV, which is 3.0 body length per second.

The maximum speed can be increased by increasing the input voltage or optimizing the geometry of the swimmers.

biological swimmer where the fast swimmer swims in smaller circle[45]. Interestingly, only clockwise rotation (when viewed from

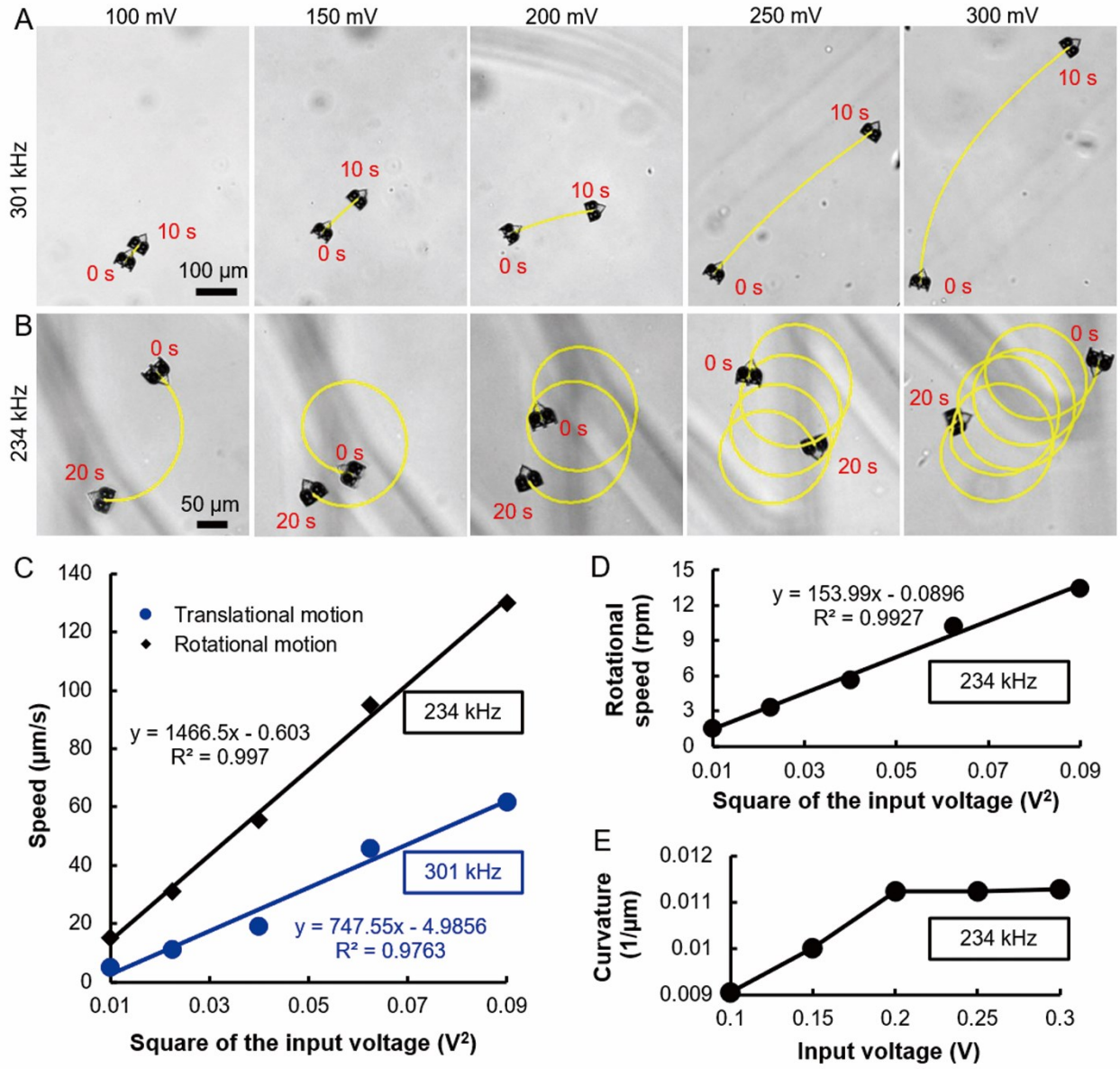

Fig. 4 The locomotion of the two-bubble micro-swimmer is controlled by ultrasound wave amplitude and frequency. (A) Translational motion of a two-bubble swimmer under the ultrasound frequency of 301kHz. The number on the top is the voltage to the function generator. The dimension of the two-bubble swimmer is indicated in Fig. 1A and B. (B) Rotational motion of a two-bubble swimmer under the ultrasound frequency of 234 kHz. In both (A) and (B), a superimposed image of two images taken at t = 0, or 10 s (20s) was shown. The yellow line is a tracked line using a time series movie taken with 50 ms between consecutive images. (C) Velocity of the micro-swimmer as a function of the voltage squared at f= 234 kHz and 301kHz. (D) Rotational speed of the circular motion as a function of the voltage squared. (E) The curvature of the rotational trajectory of the micro-swimmer as a function of the voltage. The voltage in this figure is the voltage output from the function generator which is connected to the ultrasound transducer through a power amplifier with a gain of 50 dB.

The ability of the swimmer to turn is characterized by the rotational speed of the swimmer. Fig. 4D shows that the rotational speed of the swimmer is also proportional to the voltage squared. We noticed that the radius of the circles becomes smaller as we increase the voltage (Fig. 4B). This is reflected in Fig. 4E, where the curvature initially increases with the input voltage until it reaches 200 mV and then stabilizes at around 0.011 μm^{-1} when the voltage is above 200 mV (Fig. 5E), indicating a slightly improved ability to turn through increasing the input voltage. This feature is similar to

below using an inverted microscope) of micro-swimmers was observed even when we have swept the ultrasound frequency from 100 to 1000 kHz in steps of 1 kHz. This is the frequency range that covers the resonance frequencies of both bubbles under the first volumetric mode. This indicates that the bubble on the left side with bigger opening may generate stronger propulsion force throughout the swept frequency range or the near surface hydrodynamic interaction between the swimmer and the boundary prevents the swimmer to swim CCW. Further experiments are needed to fully

understand the relation between the propulsion force, bubble geometry and ultrasound frequency and amplitude.

Taken together, the quantitative relation between the ultrasound wave amplitude and frequency lays a foundation for the control of the location of the swimmer using ultrasound waves.

Steering micro-robotic swimmer using ultrasound frequency switch

Using a sequential combination of the translational and rotational movement illustrated in Fig. 4, we are able to steer the micro-swimmer to make a left or a right turn. Figure 5A and Movie S6 shows a left turn of a micro-swimmer by alternating the ultrasound frequency between 342 and 218 kHz at the voltage of 300 mV. A micro-swimmer initially moves upward in a straight line for the first 20.8 s at the ultrasound frequency of 342 kHz. At t = 20.8s, the ultrasound frequency is switched to 218 kHz, and the swimmer immediately starts to a rotate. At t = 43 s, the frequency is switched back to 342 kHz and the swimmer immediately swims in a straight line. On the whole, the swimmer makes a left turn. Figure 5B and Movie S7 demonstrates a right turn of the same swimmer by alternating the ultrasound frequency between 328 and 234 kHz at the voltage of 300 mV. The swimmer initially moves upward in a straight line for 7.5 s at the ultrasound frequency of 328 kHz. At t = 7.5 s, ultrasound frequency is switched to 234 kHz, and the swimmer immediately rotates until the frequency is switched back to 328 kHz at t = 15 s. On the whole, the swimmer makes a right turn. Currently, the frequency switching in the experiments shown in Fig. 5 and Movie S6-7 are performed by manually operating the function generator. To make an exact right or left turn, one needs to coordinate the visualization of the swimmer and the manual switch of the frequency. We envision a computer-controlled function generator, together with a real time imaging of the swimmer to allow for an automatic navigation of the swimmer to the targeted locations. We note that visual feedback is important for a system that does not have a computer controlled feedback loop such as the one in this experiment, and also in real in vivo situation where unexpected fluid disturbance or obstacles may appear.

Materials and Methods

Fabrication and air bubble entrapment of the micro-swimmers

All micro-swimmers in this work are fabricated using NanoScribe GT2 (Nanoscribe GmbH, Germany) with a 25X objective and IP-Dip resist (Nanoscribe GmbH, Germany) on a fused silica substrate. The fabrication is a two-photon polymerization based 3D printing with a submicron resolution. The optimum micro-swimmer fabrication was realized using 40 mW laser power and 1.0×10^5 µm/s galvanometric mirror x- and y- scanning speed. The substrate with printed micro-swimmers in the liquid resist was immediately immersed into the PGMEA solution (MicroChem Corp., USA) for 30 minutes to completely dissolve the uncured resist, especially the uncured resist left in the cavity for trapping microbubbles. Then, the substrate with developed micro-swimmers were immersed into the pure Isopropyl Alcohol (Sigma-Aldrich, USA) solution for 10 minutes to clean the residue of the uncured resist. After that, the substrate with micro-swimmers was placed in the chemical hood for 10 minutes to be dried naturally. As shown in Fig. 6A, an array of two-bubble based micro-swimmers are printed on the fused silica substrate. The layered texture is due to the sub-micron pixel resolution.

Two partially covered microbubbles are automatically trapped when the dried substrate with the printed micro-swimmers is immersed into the 1XPBS (Sigma-Aldrich, USA) solution (Fig. 6B). The reasons for using 1XPBS instead of water are, (i) 1XPBS has been shown to extend the life-time of a small microbubble from few minutes to several hours. (ii) 1XPBS provides a more physiologically relevant environment compared with pure water. The micro-swimmers are now ready to be transferred to a microfluidic channel for testing.

Experimental setup

The experimental setup is shown in Fig. S1. The micro-swimmers are actuated by an immersion ultrasound transducer (V308-SU, Olympus, USA). To house the micro-swimmers, we use a microfluidic channel placed at the bottom of a transparent PMMA water tank (4 x 2 x 12 $inch^3$ cuboid) as shown in Fig. S1. Pipette tips are first used

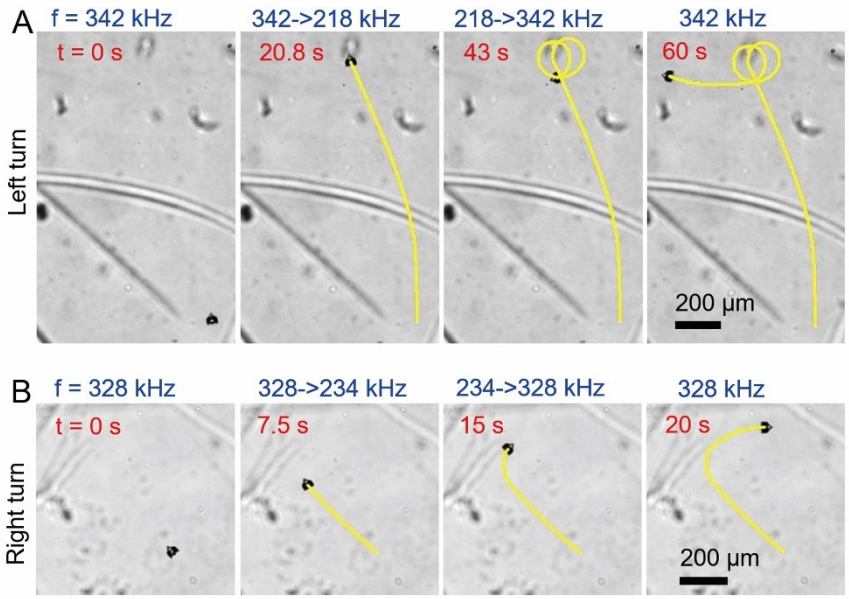

Fig. 5 A left and a right turn of a two-bubble micro-swimmer controlled by the ultrasound frequency. (A) A left turn motion is achieved by a timed frequency switch at t = 20.8 s and t = 43 s. (B) A right turn motion is achieved by timed frequency switch at t = 7.5 s and t = 15 s. In (A) and (B) the input voltage is 300 mVp-p. The dimension of the two-bubble swimmer is indicated in Fig. 1A.

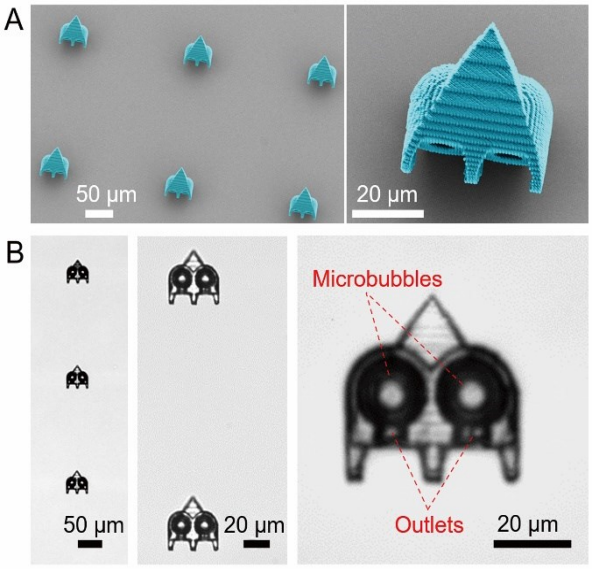

Fig. 6 Fabrication and assembly of the two-bubble swimmer. (A) SEM images of the two bubble microswimmers. The swimmers are made using a nanoscribe with a 25X objective and a two-photon polymerization method. (B) Micrographs of the anchored microswimmers submerged in 1XPBS solution with trapped bubbles. Images are taken with an inverted microscope, and 10X, 20X and 60X objective for the images from left to right. Here the swimmer has D = 18 μm, and d = 10 and 9 μm for the left and right bubble, respectively. Typically, the bubbles can be trapped for more than 2 hours in stable state.

to carefully detach the micro-swimmers from the substrate, and then the micro-swimmers are aspirated into the same pipette tip and injected into the microfluidic channel. An immersion transducer was placed into the water tank and was adjusted to directly point to the location of the microfluidic channel for efficient actuation of micro-swimmers (Fig. S1A). To power the ultrasound transducer, a function generator (AFG3021B, Tektronix, USA) is used to input a sinusoidal voltage to an E&I's 240L RF power amplifier (Electronics and Innovation, LTD, USA) with fixed gain of 50dB for all the experiments reported here. The output of the power amplifier was directly connected to the immersion transducer via a 50 ohm coaxial cable. The voltage and frequencies are read directly from the function generator. The water tank with the immersion transducer and microfluidic chip was placed on the stage of an inverted microscope (IX51, Olympus, USA) together with a high-speed fluorescence camera (Cascade 512B, Photometrics, Tucson, AZ) for the visualization of micro-swimmers (Fig. S1B).

Conclusion and Future Perspective

This paper presents a two-bubble based micro-swimmer that can be remotely powered and steered using ultrasound waves. Our work shows that the swimmer speed is linearly proportional to the ultrasound wave amplitude squared, and the swimmer can switch between linear motion to rotational motion by ultrasound frequency switch. These quantitative information opens door for future development of autonomous micro-swimmer, in which its location can be precisely programmed. To use a single ultrasound transducer to control both speed and direction of the micro-swimmer, in contrast to methods with multi ultrasound transducer or magnetic field, simplifies the control system. The compatibility of ultrasound transducer (FDA approved) allows for direct clinical applications.

Looking forward, close collaborations among scientists in fields such as physics, material science, mechanical and biomedical engineering will be required to bring the microrobots into clinical applications. To take the microrobots into clinical use, one needs to overcome several hurdles. From basic science side, advancement in understanding the relation between microstreaming flow and the locomotion of the micro-swimmer is essential for the precise location control of the micro-robots. In particular, the impact of non-Newtonian fluid (versus Newtonian fluid) on the micro-streaming behavior, as well as roles of fluid flows in the locomotion of the micro-robotic swimmers remain to be explored. From technology side, biodegradable or functionalized (for drug release) materials need to be developed to fabricate the micro-swimmer. The presented micro-swimmer has the potential to be steered autonomously integrating with ultrasound imaging.

Acknowledgements

This work is in part supported by a grant from the National Cancer Institute (Grant No R01CA221346). It is performed in part at the Cornell NanoScale Science & Technology Facility (CNF), a member of the National Nanotechnology Coordinated Infrastructure (NNCI), which is supported by the National Science Foundation (Grant NNCI-1542081). The acquisition of the nanoscribe is made possible by an NSF grant (MRI #1919653, PI; C. Ober). Wu thanks Morteza Gharib for very insightful discussions at the initial stage of this project during her visit at GALCIT Caltech, Amit Lal for advises on the use of ultrasound transducers and Paul McEuen for helpful discussions. We thank Edward Camacho, a CNF Research Support Specialist, for assistance with the Nanoscribe.

References

1 R. P. Feynman, in *APS annual meeting*, Pasadena, 1959, pp. 1–7.
2 S. Lee, J. young Kim, J. Kim, A. K. Hoshiar, J. Park, S. Lee, J. Kim, S. Pané, B. J. Nelson and H. Choi, *Adv. Healthc. Mater.*, 2020, **9**, 1–6.
3 S. Ornes, *Proc. Natl. Acad. Sci. U. S. A.*, 2017, **114**, 12356–12358.
4 I. S. M. Khalil, A. F. Tabak, K. Sadek, D. Mahdy, N. Hamdi and M. Sitti, *IEEE Robot. Autom. Lett.*, 2017, **2**, 927–934.
5 H. Ceylan, J. Giltinan, K. Kozielski and M. Sitti, *Lab Chip*, 2017, **17**, 1705–1724.
6 J. Simmchen, J. Katuri, W. E. Uspal, M. N. Popescu, M. Tasinkevych and S. Sánchez, *Nat. Commun.*, 2016, **7**, 1–9.
7 Z. Wu, L. Li, Y. Yang, P. Hu, Y. Li, S. Y. Yang, L. V. Wang and W. Gao, *Sci. Robot.*, , DOI:10.1126/scirobotics.aax0613.
8 V. Magdanz, M. Medina-Sánchez, L. Schwarz, H. Xu, J. Elgeti and O. G. Schmidt, *Adv. Mater.*, 2017, **29**, 1–18.
9 O. Yasa, P. Erkoc, Y. Alapan and M. Sitti, *Adv. Mater.*, 2018, **30**, 1–10.

10 R. Sharma and O. D. Velev, *Adv. Funct. Mater.*, 2015, **25**, 5512–5519.
11 D. Li, C. Liu, Y. Yang, L. Wang and Y. Shen, *Light Sci. Appl.*, 2020, **9**, 1–10.
12 M. Z. Miskin, A. J. Cortese, K. Dorsey, E. P. Esposito, M. F. Reynolds, Q. Liu, M. Cao, D. A. Muller, P. L. McEuen and I. Cohen, *Nature*, 2020, **584**, 557–561.
13 T. Wei, J. Liu, D. Li, S. Chen, Y. Zhang, J. Li, L. Fan, Z. Guan, C. M. Lo, L. Wang, K. Man and D. Sun, *Small*, 2020, **16**, 1–13.
14 P. Liao, L. Xing, S. Zhang and D. Sun, *Small*, 2019, **15**, 1–7.
15 J. Li, X. Li, T. Luo, R. Wang, C. Liu, S. Chen, D. Li, J. Yue, S. H. Cheng and D. Sun, *Sci. Robot.*, 2018, **3**, eaat8829.
16 H. Xie, M. Sun, X. Fan, Z. Lin, W. Chen, L. Wang, L. Dong and Q. He, *Sci. Robot.*, 2019, **4**, 1–15.
17 S. Tottori, L. Zhang, F. Qiu, K. K. Krawczyk, A. Franco-Obregõn and B. J. Nelson, *Adv. Mater.*, 2012, **24**, 811–816.
18 C. Zhou, L. Zhao, M. Wei and W. Wang, *ACS Nano*, 2017, **11**, 12668–12676.
19 W. Wang, L. A. Castro, M. Hoyos and T. E. Mallouk, *ACS Nano*, 2012, **6**, 6122–6132.
20 F. Soto, G. L. Wagner, V. Garcia-Gradilla, K. T. Gillespie, D. R. Lakshmipathy, E. Karshalev, C. Angell, Y. Chen and J. Wang, *Nanoscale*, 2016, **8**, 17788–17793.
21 M. Kaynak, A. Ozcelik, A. Nourhani, P. E. Lammert, V. H. Crespi and T. J. Huang, *Lab Chip*, 2017, **17**, 395–400.
22 D. Ahmed, T. Baasch, B. Jang, S. Pane, J. Dual and B. J. Nelson, *Nano Lett.*, 2016, **16**, 4968–4974.
23 H. Ceylan, I. C. Yasa, U. Kilic, W. Hu and M. Sitti, *Prog. Biomed. Eng.*, 2019, **1**, 012002.
24 U. Bozuyuk, Y. Alapan, A. Aghakhani, M. Yunusa and M. Sitti, *Proc. Natl. Acad. Sci. U. S. A.*, 2021, **118**, 1–10.
25 Y. Alapan, U. Bozuyuk, P. Erkoc, A. C. Karacakol and M. Sitti, *Sci. Robot.*, 2020, **5**, 1–11.
26 Q. Chen, F. W. Liu, Z. Xiao, N. Sharma, S. K. Cho and K. Kim, *IEEE Trans. Biomed. Eng.*, 2019, **66**, 3231–3237.
27 I. S. M. Khalil, D. Mahdy, A. El Sharkawy, R. R. Moustafa, A. F. Tabak, M. E. Mitwally, S. Hesham, N. Hamdi, A. Klingner, A. Mohamed and M. Sitti, *IEEE Robot. Autom. Lett.*, 2018, **3**, 1112–1119.
28 S. K. Chung and S. K. Cho, in *Proceedings of Conference, MicroTAS 2009 - The 13th International Conference on Miniaturized Systems for Chemistry and Life Sciences*, Jeju, 2009, pp. 1485–1487.
29 J. Feng and S. K. Cho, in *2013 IEEE 26th International Conference on Micro Electro Mechanical Systems (MEMS)*, IEEE, Taipei, 2013, vol. 2, pp. 63–66.
30 J. Feng, J. Yuan and S. K. Cho, *Lab Chip*, 2015, **15**, 1554–1562.
31 D. Ahmed, M. Lu, A. Nourhani, P. E. Lammert, Z. Stratton, H. S. Muddana, V. H. Crespi and T. J. Huang, *Sci. Rep.*, 2015, **5**, 9744.
32 N. Bertin, T. A. Spelman, O. Stephan, L. Gredy, M. Bouriau, E. Lauga and P. Marmottant, *Phys. Rev. Appl.*, 2015, **4**, 1–5.
33 L. Ren, N. Nama, J. M. McNeill, F. Soto, Z. Yan, W. Liu, W. Wang, J. Wang and T. E. Mallouk, *Sci. Adv.*, 2019, **5**, eaax3084.
34 J. M. McNeill, N. Nama, J. M. Braxton and T. E. Mallouk, *ACS Nano*, 2020, **14**, 7520–7528.
35 S. Mohanty, I. S. M. Khalil and S. Misra, *Proc. R. Soc. A Math. Phys. Eng. Sci.*, , DOI:10.1098/rspa.2020.0621.
36 A. Aghakhani, O. Yasa, P. Wrede and M. Sitti, *Proc. Natl. Acad. Sci. U. S. A.*, 2020, **117**, 3469–3477.
37 J. F. Louf, N. Bertin, B. Dollet, O. Stephan and P. Marmottant, *Adv. Mater. Interfaces*, 2018, **5**, 1–6.
38 F. W. Liu and S. K. Cho, *Lab Chip*, 2021, **21**, 355–364.
39 D. Ahmed, C. Dillinger, A. Hong and B. J. Nelson, *Adv. Mater. Technol.*, 2017, **2**, 1–5.
40 J. Feng, J. Yuan and S. K. Cho, *Lab Chip*, 2016, **16**, 2317–2325.
41 T. G. Leighton, *The Acoustic Bubble*, ACADEMIC PRESS, San Diego, US edition., 1994, vol. 96.
42 D. Ahmed, X. Mao, J. Shi, B. K. Juluri and T. J. Huang, *Lab Chip*, 2009, **9**, 2738–2741.
43 Y. Tomita, P. B. Robinson, R. P. Tong and J. R. Blake, *J. Fluid Mech.*, 2002, **466**, 259–283.
44 W. Lauterborn and T. Kurz, *Reports Prog. Phys.*, , DOI:10.1088/0034-4885/73/10/106501.
45 E. Lauga, W. R. DiLuzio, G. M. Whitesides and H. A. Stone, *Biophys. J.*, 2006, **90**, 400–412.
46 C. K. Tung, L. Hu, A. G. Fiore, F. Ardon, D. G. Hickman, R. O. Gilbert, S. S. Suarez and M. Wu, *Proc. Natl. Acad. Sci. U. S. A.*, 2015, **112**, 5431–5436.
47 T. Brotto, J. B. Caussin, E. Lauga and D. Bartolo, *Phys. Rev. Lett.*, 2013, **110**, 1–5.

